Mechanisms of elastic softening in highly anisotropic carbons under in-plane compression/indentation

Jean-Marc Leyssale, Guillaume Couégnat, Stéphane Jouannigot, Gérard L Vignoles

Mechanisms of elastic softening in highly anisotropic carbons under in-plane compression/indentation

Jean-Marc Leyssale[a,b,*], Guillaume Couégnat[a], Stéphane Jouannigot[a], Gérard L. Vignoles[a]

[a] *Univ. Bordeaux, CNRS, Safran, CEA, LCTS, UMR 5801, F-33600 Pessac, France*
[b] *Univ. Bordeaux, CNRS, Bordeaux INP, ISM, UMR 5255, F-33400 Talence, France*

Abstract

We present a combined experimental and computational study of the elastic behavior of a series of highly anisotropic pyrocarbons, with crystallite sizes L_a in the 2-10 nm range, under a-axis compressive load. The materials include a rough laminar and a regenerative laminar pyrocarbon, as-prepared by chemical vapor deposition and after various heat treatments up to 2600 °C, for which a-axis nanoindentation experiments have been performed, showing a significant decrease in the indentation modulus and hardness with increasing L_a (or heat treatment temperature). To rationalize this behavior, molecular dynamics simulations of the uniaxial compression of accurate atomistic models of the materials as well as pristine graphite were performed, unraveling significant out-of-plane deformations in the models with increasing compressive strain, leading to elastic softening. More precisely, significant kinks were observed around extended screw dislocation-like defects in the most disordered pyrocarbon at rather large strain levels ($\sim$ 3%). Conversely, graphite

*Corresponding author
Email address:* `jean-marc.leyssale@u-bordeaux.fr` (Jean-Marc Leyssale)

rather shows the formation of extended buckles, starting at very low strain values. Finite element modelling shows that such kinking/buckling transitions should take place in a large area under the indenter tip within usual nanoindentation conditions. Both finite element calculation and analytical approximation of the indentation modulus predict the correct trend of decreasing modulus with increasing L_a when applied with the elastic tensors computed after the buckling/kinking transitions, certainly proving the importance of the latter in the observed experimental indentation moduli.

1. Introduction

Nanoindentation (NI) is a method of choice to characterize the mechanical properties of carbon materials [1–12]. In particular, NI is extremely suited to investigate the behavior of the individual components of C/C composites, namely the carbon fibers [1, 3, 7, 10, 12, 13] and pyrocarbon (pyC) matrices [1–3, 5–9, 11]. This is especially the case of the pyC matrices which are difficult to isolate from the fibrous preforms and hence to characterize with other techniques like tensile or bending tests. However, it is agreed that compression/indentation tests are generally much more difficult to interpret in terms of the materials elastic tensors, especially when such tensors show high anisotropy [10, 14], which is generally the case of both carbon fibers and high texture pyC matrices. A particularly counter-intuitive result is generally reported when NI tests are performed with the indentation direction parallel to the graphene layers (a-axis) of highly anisotropic carbons.

2

Indeed, as reported in many studies, the obtained indentation moduli show very low values, similar to those obtained for indentation perpendicular to the graphene layers [3, 12]. For instance, according to Diss et al. [3], the longitudinal (parallel to the graphene layers) indentation modulus of PAN-based carbon fibers is of 27 GPa, close to the transverse elastic constant ($C_{33} \approx$ 36 GPa) but lower by more than one order of magnitude than the in-plane elastic constant ($C_{11} \approx 500$ GPa). Values of the same order of magnitude were reported in many other studies for various commercial carbon fibers [7, 12] and high-texture pyC carbon matrices [3, 7–9].

To explain the low elastic moduli obtained from NI experiments, Diss et al. postulated a load transfer close to the indenter tip, from in-plane (C_{11}) to out-of-plane (C_{33}) compression, giving rise to the separation of graphite layers in a so-called "wedge effect" [3]. The formation of kink bands and nano-buckling are often considered as deformation modes in the literature [4, 7, 12]. A similar nanoscale buckling was evidenced by synchrotron X-ray diffraction for a carbon fiber under bending load [15]. Recent work by Barsoum and co-workers based on indentation experiments and molecular dynamics (MD) simulations applied to a range of materials from plastic cards and steel to Ti_3SiC_2 and graphite, have uncovered the universality of the buckling behavior, called ripplocations, of layered materials under longitudinal compression [16–19]. Nano-buckling/kinking was also observed recently in MD simulations of the uniaxial longitudinal compression of pyC models generated by engineering arrays of screw dislocations in graphite [20] and of a layered molecular crystal [21].

Despite these recently published studies on the compression behavior of

highly anisotropic materials, so far, a clear picture on the effect of intrinsic disorder on the compression properties and mechanism is still lacking. In what follows we investigate the behavior under longitudinal compression of a series of high-textured pyC samples showing crystallite sizes L_a in the 2-10 nm range and for which accurate atomistic models are available. Materials are tested using NI and compared to MD simulations and finite element modelling (FEM).

2. Materials

The materials considered here have been described in details in former publications [22, 23]. They comprise a rough laminar (RL) pyrocarbon prepared by isothermal-isobaric chemical vapor infiltration (CVI) from a methane/propane mixture at a temperature in the 1000-1100 °C range (PyC-1 in Ref. 22) and a regenerative laminar (ReL) pyrocarbon obtained by infiltrating a silica woven preform with a pure methane precursor [23] at 1050 °C. Samples of the ReL pyC heat treated for one hour at various temperatures in an induction furnace under high vacuum are also considered. The heat treatment temperature (HTT) ranges from 1300 °C to 2600 °C. A detailed characterization of these materials - including X-ray diffraction, neutron diffraction, selected area electron diffraction (SAED), He pycnometry, H-content measurements by Secondary Ion Mass Spectroscopy coupled to Elastic Recoil Detection Analysis (SIMS/ERDA), Raman spectroscopy and high-resolution transmission electron microscopy (HRTEM) - is available in Ref. 23. Some important microstructural parameters are summarized in table 1.

Table 1: Summary of microstructural parameters including the in-plane (L_a) and out-of-plane (L_c) coherence lengths and interlayer distance (d_{002}) extracted from the 10 band (L_a) and 002 peak (L_c, d_{002}) of the X-ray diffraction patterns, the orientation angle (OA) obtained from selected area electron diffraction (SAED) patterns, the hydrogen content from secondary ion mass spectroscopy and elastic recoil detection analysis (SIMS/ERDA), the density (d) from He pycnometry and the full width at half maximum of the Raman D band ($FWHM_D$). L_a values for the ReL pyC treated at 1900 °C and above (in parentheses in the table) have been obtained by fitting the evolution of L_a with $FWHM_D$ and extrapolation to low $FWHM_D$ values (see Fig. S1 in the supporting information).

Material	L_a(nm)	L_c(nm)	d_{002}(nm)	OA (degrees)	H (at. %)	d(g/cm^3)	$FWHM_D$(cm^{-1})
RL	4.6	5.2	0.345	22	0.7	2.12	83
ReL	2.6	2.9	0.346	40	2.5	2.11	203
ReL$_{1300}$	3.1	3.8	0.347	43	-	2.16	147
ReL$_{1500}$	4.1	6.3	0.345	30	-	2.18	116
ReL$_{1700}$	6.1	13.3	0.343	27	-	2.18	65
ReL$_{1900}$	(8.2)					2.18	42
ReL$_{2100}$	(10.6)					2.18	30
ReL$_{2600}$	(8.4)						41

One can observe in table 1 that the size of coherent domains in the ReL pyC significantly increases with heat treatment; for instance, the in-plane coherence length L_a increases from 2.6 nm to about 10 nm after heat treatment above 2000 °C. Meanwhile, the anisotropy of the material decreases as shown by the decrease in the orientation angle (OA), defined as the full width at half maximum of the 002 arcs in SAED patterns, from about 40 degrees for the as-prepared material to about 27 degrees after treatment at 1700 °C. Another important effect of the heat treatment in the ReL pyC is the very significant decrease in the full width at half maximum of the Raman D band (FWHM$_D$) dropping from about 200 cm^{-1} for the as-prepared material to about 30-40 cm^{-1} after heat treatment above 2000 °C. As shown in Fig. S1 of the supporting information, the good correlation observed between L_a and FWHM$_D$ ($L_a \propto 1/\text{FWHM}_D^{0.75}$) was used to predict values of L_a at high HTT (T $\geq$ 1900 °C) for which X-ray diffraction experiments have not been performed. The density increases from 2.11 g/cm^3 for the as-prepared ReL pyC to a plateau value of 2.18 g/cm^3 after heat treatment at 1500 °C. These values are close to the one of crystalline graphite and no porosity could be detected on high-resolution TEM images [22, 23]. About 2.5 at. % and 0.7 at. % of hydrogen are present in the as-prepared ReL and RL pyCs, respectively. Hydrogen is released with heat treatment as early as in the 1300 °C treatment. Overall, we observe that the RL sample has similar parameters to those of the ReL pyC treated at temperatures in the 1500-1700 °C range.

Atomistic models of the as-prepared pyCs and of the ReL pyC heat treated up to 1700°C were generated using the image guided atomistic reconstruction technique [23, 25, 26]. The structural/textural features of these

Table 2: Elastic constants (in GPa) of the pyrocarbon models obtained from MD simulations [24]. C_{11}, C_{33}, C_{12} and C_{13} are mean values from tensile and compressive simulations. C_{44} and C_{66} are obtainded from shear simulations. Data for graphite where index 1 corresponds to the zigzag (ZZ) direction are given for comparison.

Model	C_{11}	C_{33}	C_{12}	C_{13}	C_{66}	C_{44}
Graphite (ZZ)	901	34	213	4	349	0.5
RL	583	24	120	26	235	9.4
ReL	489	25	94	30	190	13.4
ReL_{1300}	557	30	112	33	225	15.4
ReL_{1500}	603	28	115	27	244	9.5
ReL_{1700}	600	24	100	21	239	7.2

models have been validated against experimental structure factors ($S(q)$), pair distribution functions up to large interatomic distances (3 nm), including the highly discriminatory $r^2G(r)$ functions, as well as properties measured on HRTEM images (fringe length, tortuosity and orientation statistics), showing good agreement[23]. The models contain small graphene layers, in agreement with L_a values, connected via both in-plane grain boundaries, formed by pentagons and heptagons, and extended out-of-plane cross-links, mostly under the form of screw dislocations. They count between 1.7 to 2.8 % of fourfold (sp^3) C atoms, mostly located in cross-links. The number of defects with respect to crystalline graphite (also called disorder in what follows) decreases with increasing HTT and obviously with increasing L_a. By construction, low L_a values imply large amounts of grain boundaries and crosslinks. Their elastic tensors, summarized in table 2, were determined in Ref. 24 using MD

and the same interatomic potential that was used to generate the models[23] and will be used in this work to determine their behavior under compression (see section 3.2 below), for consistency. One observes that in-plane elastic constants - C_{11}, C_{12} and C_{66} - show values in relatively narrow ranges for all pyC models but as-prepared ReL, accounting for roughly about 60 % of the corresponding values for graphite. The lower values obtained for the as-prepared ReL pyC were attributed to the presence of H atoms at domain edges [24]. Constants involving interlayer couplings (C_{13} and C_{44}) are significantly larger for the pyCs (by about one order of magnitude) than for graphite, due to the presence of interlayer covalent bonds in the pyC models. Overall, we observe that both C_{11} and C_{66} increase with HTT for ReL pyCs, which is consistent with the observed increase in coherence length L_a.

3. Methods

3.1. Nano-indentation

In order to determine hardness and elastic moduli of pyrocarbons, a Nanotest NTX-P3 instrument from Micromaterials Ltd has been used with a Berkovich (three-sided pyramidal) diamond indenter. A 3.5 mN peak load was applied with a loading/unloading rate of 0.175 mN/s. The initial contact load was of 0.01 mN and the holding period at peak load was 30 s. The tests were performed in the direction parallel to the graphene planes. An average of 12 independent measurements were performed per sample. All nanoindentation tests were performed at room temperature.

The elastic moduli were determined from the indentation curves by using

a method originally proposed by Sneddon [27] :

$$P = E_r \frac{2 \tan \alpha}{\pi} h^2 \tag{1}$$

where P is the load, h is the penetration depth, $\alpha = 70.3°$ is the effective cone semi-angle and E_r is the reduced modulus:

$$\frac{1}{E_r} = \frac{1 - \nu^2}{E} + \frac{1 - \nu_i^2}{E_i} \tag{2}$$

where E and E_i are the Young's Modulus of the sample and of the indenter respectively, and ν and ν_i are the Poisson's ratio of the sample and of the indenter respectively. The tip properties are $E_i = 1141$ GPa and $\nu_i = 0.07$. The indentation modulus M is thus defined as

$$\frac{1}{M} = \frac{1 - \nu^2}{E} = \frac{1}{E_r} - \frac{1 - \nu_i^2}{E_i}. \tag{3}$$

Hardness is defined as the ratio of the load over the contact area A at maximum load:

$$H = \frac{P}{A}. \tag{4}$$

3.2. Molecular dynamics simulations

Elastic properties of the pyC models are computed as in former work [24, 28, 29] using MD simulations with the second-generation reactive empirical bond order potential (REBO) [30] modified to incorporate van der Waals interactions between non-bonded atoms according to the adaptive scheme developed by Stuart *et al.* [31]. General to these simulations is the use of the velocity Verlet algorithm [32] to integrate the equations of motion, operated with timesteps of 0.25 and 0.5 fs for systems containing and not containing hydrogen, respectively, and an Andersen thermostat [33] with collision

frequency 10^{12} s^{-1} to fix the temperature at 300 K. Prior to deformation simulations, the systems are fully relaxed at zero stress using MD in the NPT ensemble at 300 K for 100 ps with an anisotropic weak-coupling (Berendsen) barostat [34].

Uniaxial compression tests are performed in constrained conditions (see Ref. [24]), meaning that the cell dimensions in the orthogonal directions and cell angles are held fixed. The cell deformation along the compression direction is performed by applying an infinitesimal homothetic transformation to the system's coordinates after every MD integration step at a very low engineering strain rate of 4×10^7 s^{-1}. Strain rates of 4×10^6 s^{-1} and 4×10^8 s^{-1} are also considered in some cases to evaluate the effect of strain rate on the compression properties. As will be discussed below, compression induces a significant change in the elastic behavior for all the models, due to the buckling/kinking of the graphene layers. The elastic constants of the buckled/kinked models are computed slightly above the transition in two steps: i) the cell dimensions in the orthogonal directions are relaxed in the NPT ensemble at 300 K for 100 ps; ii) the elastic tensors are computed from a combination of uniaxial tensile tests, uniaxial compression tests and shear tests performed at a constant engineering strain rate of 4×10^8 s^{-1}. Shear strain is applied through the use of Lees-Edwards boundary conditions [35]. In what follows direction 1 corresponds to the compression direction while directions 2 and 3 designate the orthogonal in-plane (a-axis) and out-of-plane (c-axis) directions, respectively.

3.3. Finite elements modelling

The indentation response of the materials is also simulated using a 3D FEM model, using Abaqus 6.12, fed by the elastic tensors computed with MD simulations. The use of a full three-dimensional geometry, rather than the usual axisymmetric assumption, is required here to account for the anisotropy of the elastic properties of the pyC.
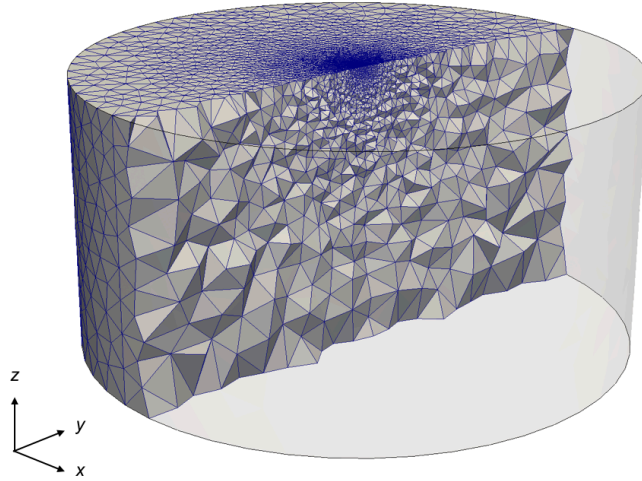

Figure 1: Cut-view of the finite element mesh used for the simulation of the indentation response of the pyC materials.

The geometry of the sample and the mesh used in the following are illustrated in Fig. 1. Practically, the domain is a cylinder of radius and height of 12.5 μm. The computational domain is chosen large enough so that the boundary conditions do not influence the results. The mesh size is heavily refined on the top surface, where the indenter will imprint the sample. The minimal element length is 10 nm just below the indenter. The indenter is

modelled as an analytical rigid conical surface with a half-angle of 70.3°, which gives the same area-to-depth ratio as a Berkovich indenter tip. The interaction between the indenter and the sample is modelled using a hard frictionless contact. The simulations are controlled in displacement where the bottom surface of the domain is kept fixed and the vertical displacement of the indenter is gradually applied in the z–direction. The maximal indentation depth is set to 250 nm.

The load-displacement (P–h) curve of the indenter is eventually retrieved to derive the reduced modulus using Eq. 1. The size of the domain and the mesh refinement were calibrated thanks to a preliminary convergence study using a reference isotropic medium. Yet, as previously reported in [36], there could still exist a difference of up to 10% on the indentation load P between FEM results and Sneddon's solution depending on the Poisson's ratio of the material.

A local coordinate system is attached to the material so that the direction in which the indentation modulus is sought matches with the z-axis of the FE model. The effect of geometric non-linearity was found to be negligible while causing convergence difficulties, and, therefore, has not been included in the results reported hereafter.

4. Results

4.1. Nanoindentation tests

We first describe the results of the nano-indentation experiments performed on all the pyC samples along the longitudinal direction. The loading-unloading curves of the different pyC samples are shown in Fig. 2. It is
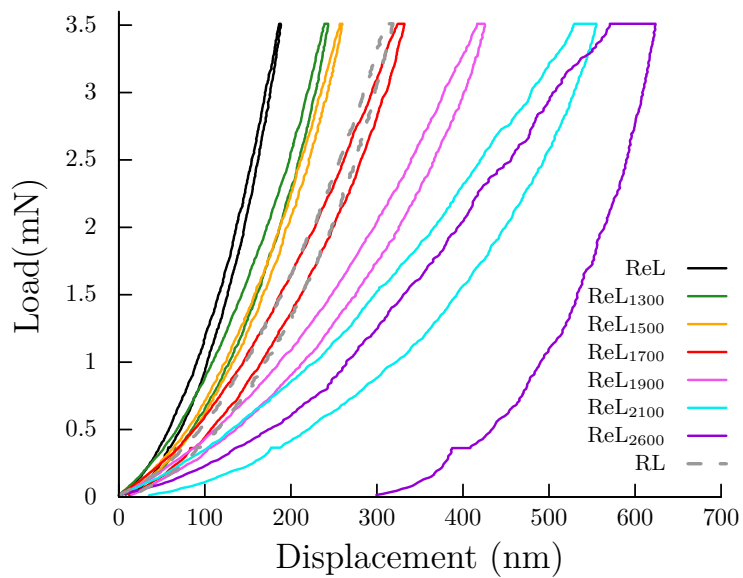
Figure 2: Experimental nanoindentation load-displacement curves. Black: as-prepared ReL pyC; grey-dashed: as-prepared RL pyC; colors: ReL pyC heat treated at 1300 °C (green), 1500 °C (orange), 1700 °C (red), 1900 °C (magenta), 2100 °C (cyan) and 2600 °C (violet).

clear that the penetration depth of the indenter at maximum load increases significantly with the HTT (by a factor of 5 from the as-prepared ReL pyC to the 2600 °C heat treated pyC), indicating a significant reduction of stiffness and hardness with heat treatment. It is also noticeable that all the materials show a perfectly elastic behavior, with no permanent deformation after unloading, for HTTs up to about 2100 °C. Conversely, at 2600 °C, an important deformation remains, despite the relatively low value of the peak load (3.5 mN). The behavior of the as-prepared RL pyC under the indenter is extremely similar to the one of the ReL pyC heat treated at 1700 °C.
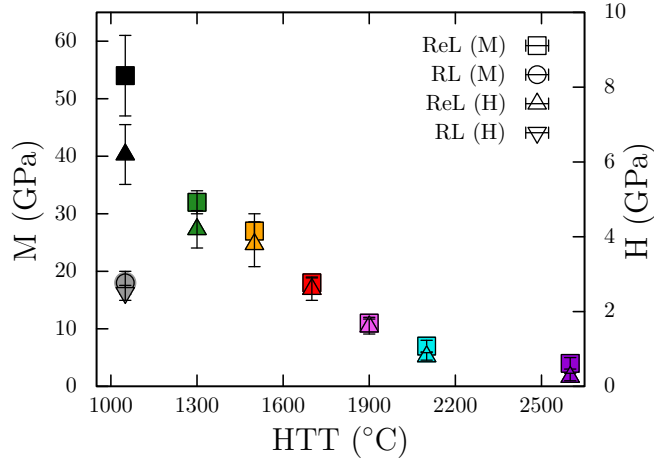

Figure 3: Evolutions of the indentation modulus (M) and hardness (H) with HTT (the HTT value for the as-prepared pyCs is arbitrarily set to the preparation temperature of the ReL pyC). Same color code as in Fig. 2.

Indentation moduli (M) and hardnesses (H) derived from the indentation curves are shown as a function of the preparation or heat treatment temperature in Fig. 3. As expected from the indentation curves, both the modulus

and hardness decrease significantly with HTT, showing very similar evolutions. More specifically, M decreases from 55 ± 5 GPa for the as-prepared ReL pyC to 4 ± 1 GPa after heat treatment at 2600 °C, while H decreases from 6.4 ± 0.7 GPa to 0.25 ± 0.1 GPa. Again, values for the RL pyC (M = 18 ± 2, H = 2.5 ± 0.2) correspond to those of the ReL pyC treated at 1700 °C.
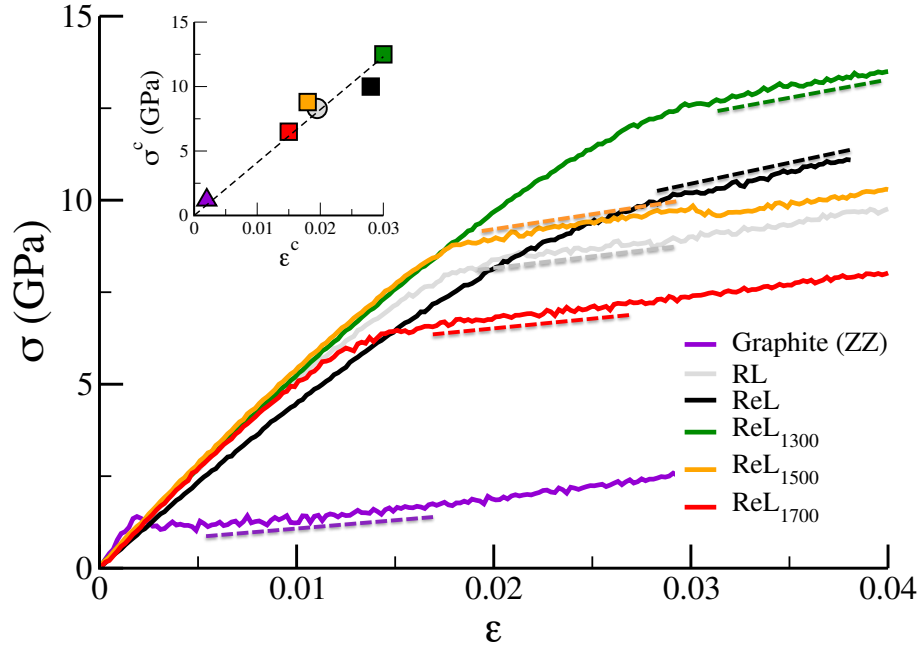
4.2. Compression simulations

Figure 4: Compression curves (stress (σ) versus strain (ε)) obtained from MD simulations of a-axis compression. Dashed lines indicate a second domain of linearity above a softening transition in the elastic behavior marked by a significant change in the slopes of the curves. Critical stresses (σ^c) and strains (ε^c) at which the transitions are observed are given in the inset (dashed line in the inset is a linear guide to the eye). Same color code as in Fig. 2.

Longitudinal compression curves obtained from MD simulations for the ReL pyC models, including the as-prepared (ReL) and heat-treated materials at 1300 °C (ReL$_{1300}$), 1500 °C (ReL$_{1500}$) and 1700 °C (ReL$_{1700}$), the RL pyC model (RL) and graphite along the zigzag direction (ZZ) are shown in Fig. 4. As can be seen, stress increases strongly with strain at low strains, with a linear dependence corresponding to the C$_{11}$ values given in table 2. However, at some critical strain values (ε^c), a change in slope is obtained for all models, leading to a much more compliant behavior, even though maintaining a linear dependence of stress with respect to strain, suggesting a linear elastic behavior. Interestingly, as shown in the inset, both critical strain and stress seem to decrease with decreasing disorder from the most disordered ReL and ReL$_{1300}$ pyC to graphite.

Unloading simulations were also performed for all the models, starting from the largest strains shown in Fig. 4, back to zero strain. Loading and unloading curves were found to superimpose well, leading to zero permanent stress/strain after unloading and no apparent plastic deformation (see Fig. S2 in the supporting information), confirming well the fully elastic nature of the compression up to the reported strain levels (4 %).

The observed change in compression behavior is clearly related to a change in the loading mechanism at the microscopic scale. Fig. 5 shows snapshots of the graphite, ReL$_{1700}$ and ReL$_{1300}$ models at rest (Fig. 5 (a,d,g)), at the critical strains (ε^c) characteristic of the slope change (Fig. 5 (b,e,h)) and well above (Fig. 5 (c,f,i)). From the snapshots in Fig. 5(a-c) it is evident that the change in the elastic behavior of graphite is related to the buckling of the graphene layers along the compression direction. In the early stages of the
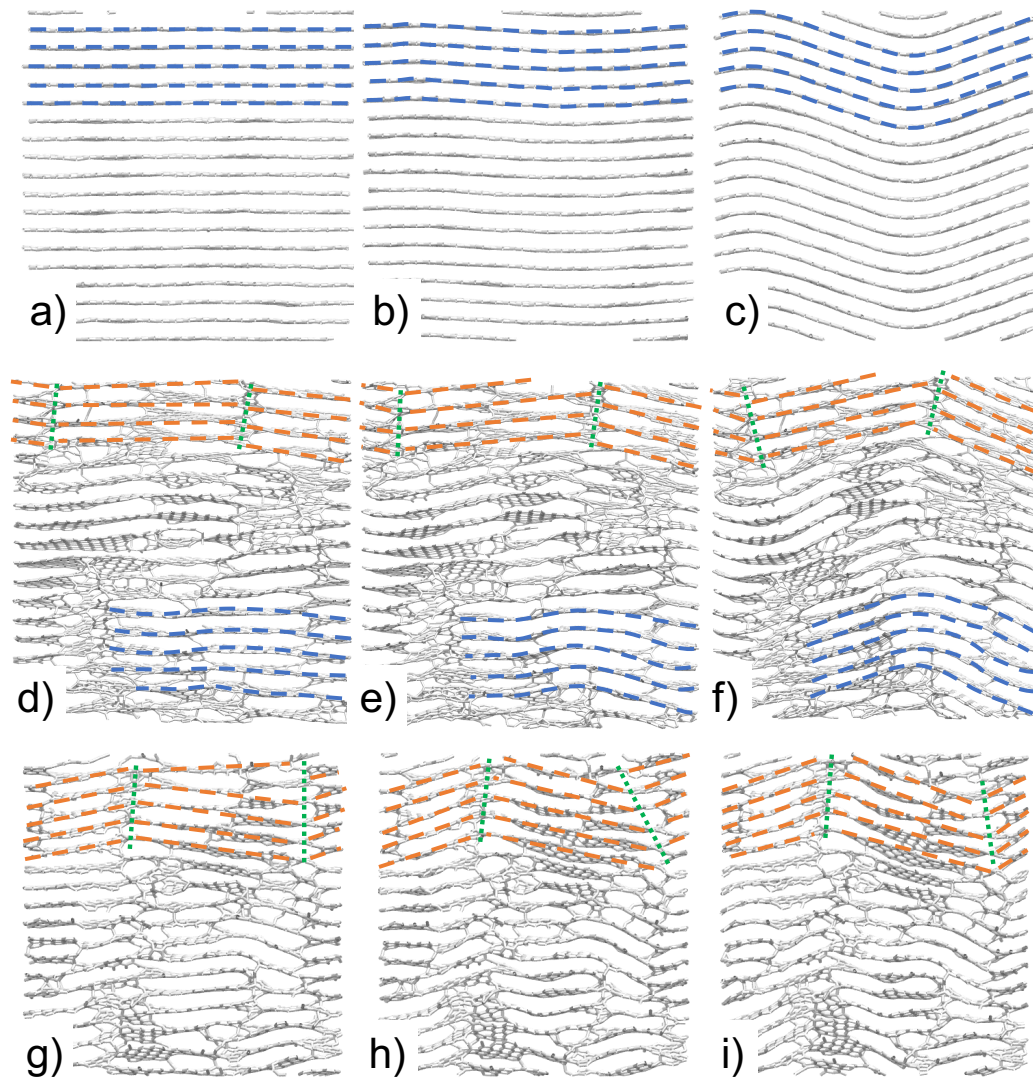
Figure 5: Snapshots of (a-c) graphite, (d-f) ReL_{1700} and (g-i) ReL_{1300} models at different stages of longitudinal compression (horizontal direction). Strain values are (a) 0, (b) 0.002, (c) 0.04, (d) 0, (e) 0.015, (f) 0.04, (g) 0, (h) 0.029 and (i) 0.04. Only 2 nm thick slabs are shown for clarity. Superimposed dashed lines are guides to the eye to visualize the formation of kinks (orange) around extended screw dislocations (green) or buckles (blue) during compression. The full compression trajectories are available as supporting movies M1 (graphite), M2 (Rel_{1300} adn M3 (ReL_{1700}).

test, loading consists of in-plane compression and the stiffness response corresponds well to graphite's C_{11}. At a strain of about 0.2 %, some fluctuations in the out-of-plane deformation of the layers leads to a deformation mode which deviates from pure a-axis compression and progressively increases the graphene layers curvature. This eventually results in a buckled/rippled texture with progressively increasing amplitude, yet showing a unique oscillation within the model's width (Fig. 5(c)). A similar buckling (or ripplocation) transition was recently observed by Lafourcade et al. in MD simulation of the triaxial compression of a large graphite model [37] where a large bump in the stress-strain curve was observed around the buckling transition as well as slightly larger critical ε^c and σ^c values. Similarly, Freiberg et al. also observed such a stress bump in their indentation simulations, suggesting that ripplocation is an activated nucleation process, allowing for subsequent stress release under further indentation [18]. We show in Fig. S3 the effect of strain rate on the compression curve of graphite. While stress bumps indeed appear at large strain rates, they do not exist under more realistic strain rates and can thus certainly be considered as strain rate artifacts, espcecially in NI for which experimental deformation rates are considerably lower than those used in MD simulations. Fig. S3 also shows that the strain rate used here is sufficiently low to avoid most of this artefact.

Fig. 5(g-i) shows snapshots of the ReL_{1300} pyC model, one of the most disordered carbon investigated in this work, with smallest L_a and largest amount of cross-linking, along the compression simulation. Unlike graphite, we do not observe here significant buckling within the graphene layers. However, we can clearly see an increase in the misorientation angle at extended out-

of-plane defects (screw dislocations) between different well stacked graphene domains with increasing strain. A major difference with graphite is that kinks already exist at rest in the material (see Fig. 5(g)), hence the transition is much softer and progressive for the disordered pyC models than for graphite. Moreover, as shown in the inset to Fig. 4, the more disordered the material is, the more delayed and the less pronounced the transition is. Indeed, kinking transitions for the ReL and ReL$_{1300}$ models, supposedly the most disordered with shortest L$_a$ and largest OA and FWHM$_D$, show rather continuous transitions between the compressive and kinking deformations with largest slope changes around strain values of ~ 3 %. Conversely, the most ordered pyC model, ReL$_{1700}$, shows a stiff transition at ~ 1.3 % strain. Snapshots of the evolution of the ReL$_{1700}$ pyC model during compression (Fig. 5(d-f) shows that this intermediate behavior is due to the concomitant development of buckling and kinking in this material.

In an attempt to quantify the out-of-plane deformations observed in Fig. 5 and responsible for the elastic softening of the stress-strain curves (Fig. 4) we show in Fig. 6 an analysis of the c-axis non-affine displacements. Non-affine displacement fields have been shown to be extremely suitable tools in characterizing local deformations in glasses [38, 39] and were recently used to characterize the elastic or viscoelastic behavior of hard and soft porous carbons [40]. The α-component ($\alpha = x, y$ or z) of the non-affine displacement of a given atom is simply defined as $u_\alpha^{\text{na}} = r_\alpha^{\text{new}} - r_\alpha^{\text{old}} - u_\alpha^{\text{a}}$ where r_α^{new} and r_α^{old} represent the position of the atom prior to and after the deformation, and u_α^{a} is the affine displacement of the atom defined as $u_\alpha^{\text{a}} = r_\alpha^{\text{old}} \times \frac{L_\alpha^{\text{new}} - L_\alpha^{\text{old}}}{L_\alpha^{\text{old}}}$, L_α^{new} and L_α^{old} being the lengths in the α direction of the deformed and undeformed
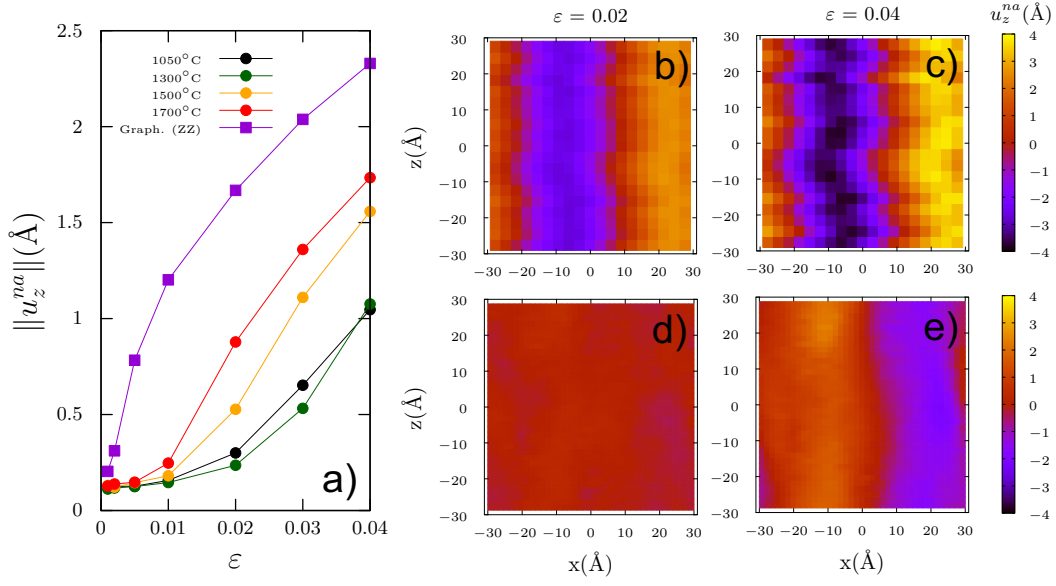
Figure 6: Out-of-plane (*c*-axis) non-affine displacements of the compressed models. (a) Evolution with compressive strain of the average norm of the non-affine displacements. (b-e) 2D maps of the average non-affine displacements in the x-z plane, where x and z directions correspond to the compressed a-axis and the c-axis, respectively (b: ZZ graphite at $\varepsilon = 2\%$; c: ZZ graphite at $\varepsilon = 4\%$; d: ReL$_{1300}$ at $\varepsilon = 2\%$; e: ReL$_{1300}$ at $\varepsilon = 4\%$). The residual ~ 0.1 Å displacement at 0 strain corresponds to the average thermal vibrations along the *c*-axis.

cell, respectively.

Fig. 6(a) shows the evolutions of the average norm of the non-affine displacements in the z direction $\|u_z^{na}\|$ as a function of strain for ZZ graphite and all the ReL pyC models. We see that $\|u_z^{na}\|$ increases with ε for all models, confirming the scenario of a deformation along the c-axis during a-axis compression. In the case of graphite, $\|u_z^{na}\|$ increases strongly with ε in the early stages, then becomes less pronounced with increasing ε. Conversely, $\|u_z^{na}\|$ of as-prepared ReL and ReL_{1300} models increase very slowly, or even remain constant, with strain at low strains, then show a superlinear increase at higher strain, typically around the critical strain $\varepsilon^c \sim 3\%$. As expected, ReL_{1500} and ReL_{1700} show an intermediate behavior with a transition at $\varepsilon^c \sim$ 1.7% between the slow increase at low strains observed for more disordered pyC models and the strong yet sublinear increase typical of graphite at larger strains.

Fig. 6(b-e) shows 2D maps of the average non-affine displacement u^{na} in the plane defined by the compression direction (a-axis) and the c-axis for graphite at strains of 2 % (Fig. 6(b)) and 4 % (Fig. 6(c)), and the ReL_{1300} pyC at strains of 2 % (Fig. 6(d)) and 4 % (Fig. 6(e)). All the maps show the presence of a unique displacement wave along the models' widths, in agreement with the observations of Fig. 5. Furthermore, we can see that the amplitude of the c-axis deformations is considerably larger for graphite than for pyC ReL_{1300}, especially at 2% strain where the wave is already extremely pronounced for graphite and almost unnoticeable for the pyrocarbon.

Another convenient way to characterize the loading mechanism is through the analysis of diffraction patterns, which are computed from the atomistic

models using the Debye equation:

$$I(Q) = \sum_i \sum_j f_i f_j \frac{\sin(Qr_{ij})}{Qr_{ij}} \tag{5}$$

where I is the scattered intensity, Q the scattering vector, f_i and f_j are the atomic scattering factors of atoms i and j, respectively, and r_{ij} the interatomic distance. All calculations are done using the Debyer software [41], with proper accounting for the periodic boundary conditions. A *sinc* damping function is applied in the case of graphite to avoid truncation artifacts. Neutron weighting is considered with scattering factors taken from Sears et al. [42].

Fig. 7(a) shows the evolution of the 002 peak of graphite as a function of its compressive strain in the ZZ direction. We can see a progressive broadening of the peak with increasing strain, consistent with the reduction of the coherence length along the c-axis (L_c). The peak position is also progressively shifted to larger Q which indicates a reduction in the interlayer distance d_{002}. This is definitive evidence that the compressive load, at least part of it, is transferred from a-axis mode to c-axis mode. As shown in Fig. 7(b), a similar behavior is observed in the case of the ReL pyC, even though much broader 002 peaks are observed, as expected for a material with "crystallite" sizes in the nm range. Also, the shifting of the peak position seems to only be observed at large strains while a regular shift with strain is observed for graphite.

Evolutions with strain of the apparent interlayer distances d_{002}, computed from the peak positions using Bragg's equation: $d_{002} = 2\pi/Q$, are given in Fig. 7(c). In the case of graphite, d_{002} is conserved at very low strains, up to about 0.2 %, then follows a strong linear decrease, almost perfectly
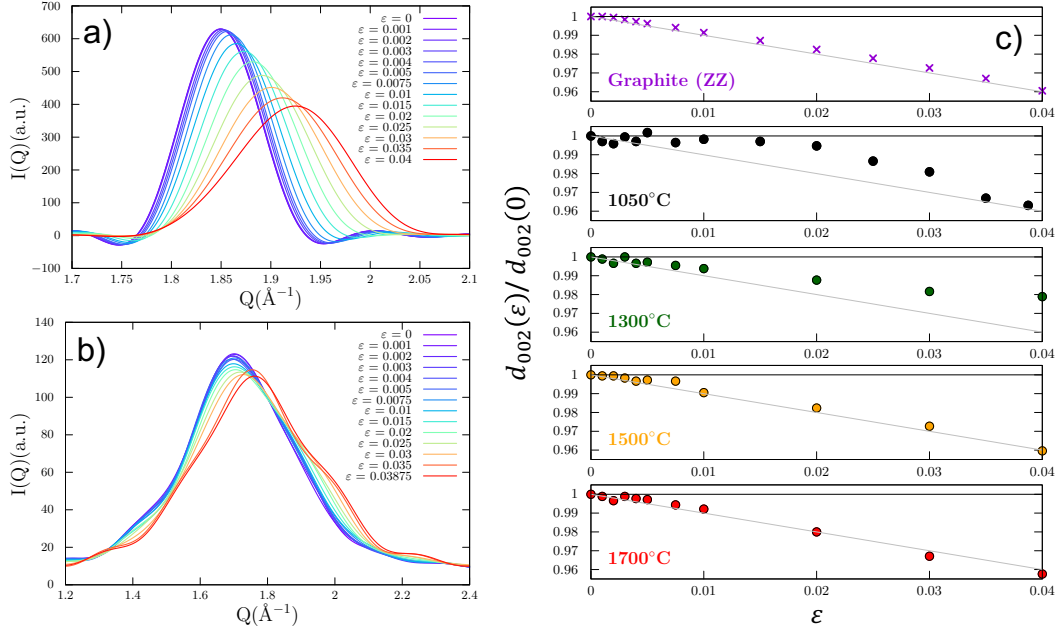
22

Figure 7: Evolution of the simulated neutron diffraction 002 peak shape as a function of
a-axis compressive strain for (a) ZZ graphite and (b) as-prepared ReL pyC model. (c)
Evolution of the 002 peak position with applied strain for ZZ graphite and the ReL pyC
as-prepared (1050°C) and for HTTs of 1300, 1500 and 1700°C. Black and grey lines in
(c) are the theoretical values expected for pure in-plane (a-axis) and out-of-plane (c-axis)
compressions, respectively.

fitting the line of pure c-axis compression. In contrast, for the as-prepared (1050°C) ReL pyC, d_{002} remains unchanged up to a much larger strain value of about 2 %, then shows an abrupt decrease around the kinking transition strain and eventually reach the pure c-axis regime at large strains of about 3.5 %. The behavior of the ReL pyC at 1300°C HTT is similar to the one of the as-prepared material, with the only noticeable difference being that pure c-axis compression is not reached by the end of the compression simulation. Conversely, at higher HTTs, d_{002} evolves with strain in a very similar way than was observed for graphite, thus confirming the significantly different loading mechanisms observed at low HTT (1050 and 1300°C) and high HTTs (1500 and 1700°C).

4.3. Nanoindentation modelling

Fig. 8 shows the distribution of strain at maximum indentation depth (250 nm), obtained from FEM for graphite in the ZZ direction and the 1300 °C ReL pyC. These data were obtained using the elastic tensors provided in table 2. The current FEM model makes use of a small deformation hypothesis and hence, cannot account for such non-linear mechanisms as the identified buckling mechanism. However, as shown in Fig. 8, the obtained strain distributions show values that are exceeding the critical buckling strain ε^c, 0.2 % and 3% for graphite and the pyC, respectively, in large areas of about one (pyC) to several (Graphite) μm under the tip. The MD results presented above indicate that these large domains should have undergone the buckling transition if permitted by the model and that their elastic behavior should be much softer.

Fig. 9 shows the apparent elastic constants C_{11}^k computed after the kink-
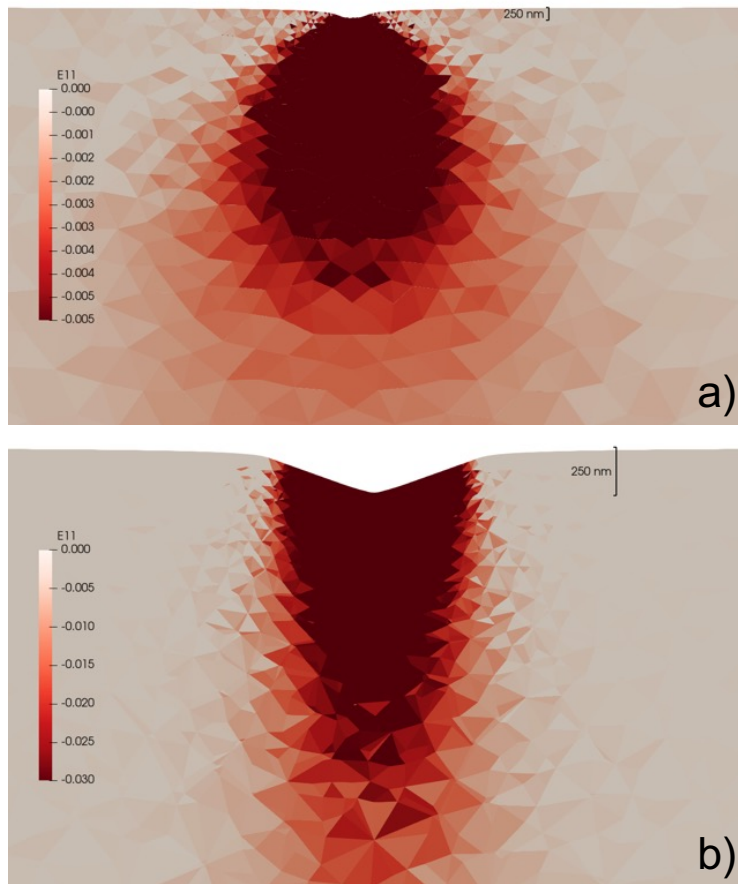
Figure 8: 2D map of the longitudinal strain during a-axis indentation of (a) ZZ graphite and (b) ReL_{1300} pyC obtained from finite element modelling.

ing/buckling transitions (the considered strain ranges for the linear fits are indicated by dashed lines in Fig. 4). Corresponding numerical values are given in table 3. Interestingly, one can notice that unlike C_{11}, which increases with increasing order (e.g. with increasing temperature for the ReL pyC), C_{11}^k is maximal for the as-prepared ReL pyC (123 GPa) and progressively decreases with increasing HTT down to a value of 63 GPa for the ReL_{1700} model, a value equal to the one obtained for graphite. These values are clearly in line, even though larger by factors of 2-3, with the experimental indentation moduli (M_1^{Exp}), showing a decrease in the modulus of the ReL pyC from 55 GPa as-prepared to 18 GPa after heat treatment at 1700°C.

To go further in the comparison between the experimental indentation moduli and the elastic properties of the kinked/buckled models we computed the full elastic tensors of the models right after the transition. First, all the models were relaxed at values of the compressive strain ε_{11} (direction 1) slightly above the critical strain ε^c (e.g. at the beginning of the second linear domain) and with constant stress conditions ($\sigma_{22} = \sigma_{33} = 0$) in the normal directions to release any strain in the latter. Then, tensile, compressive and shear tests were performed to compute the complete elastic tensors of the kinked/buckled models. Note that because of kinking/buckling, the symmetry of the system is no longer transverse isotropic but orthotropic. Therefore, a total of nine independent elastic constants has to be considered, instead of six for a transverse isotropic material. Having defined the axes, the definitions of $C_{\alpha\alpha}^k$ and $C_{\alpha\beta}^k$ with α and $\beta \in (1:3)$ is obvious (the k superscript indicates that the constants correspond to the materials with a kink/buckle along direction 1). Similarly, we define C_{44}^k, C_{55}^k and C_{66}^k as the shears in
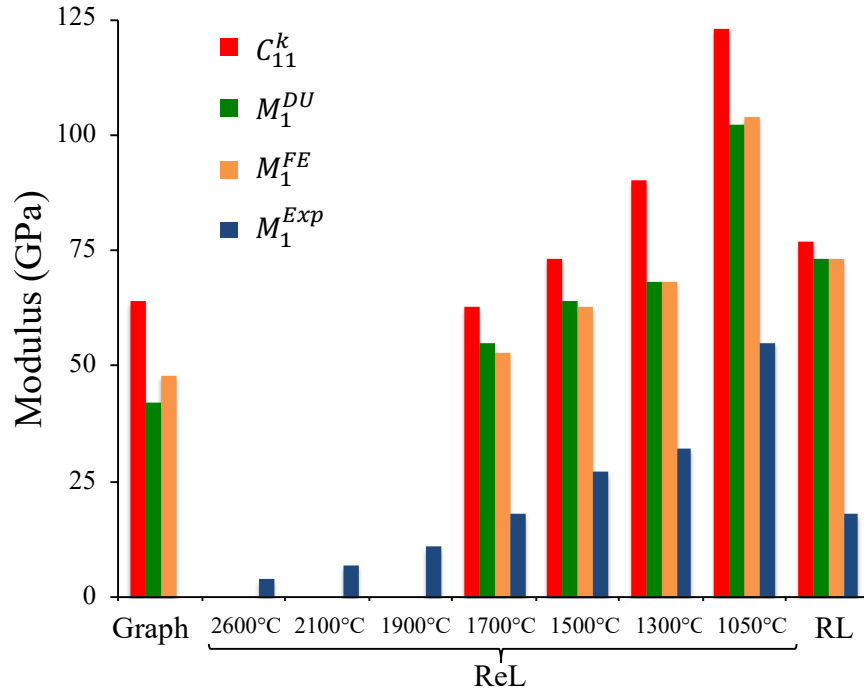
Figure 9: Measured and predicted longitudinal compressive elastic constants and moduli. Shown are C_{11}^k (red) and indentation modulus M_1 computed with the Delafargue and Ulm approximation[43] (green), finite element simulations (orange) and from nanoindentation experiments (blue).

the (1,3), (2,3) and (1,2) planes, respectively. The complete tensors were obtained from linear fits of compressive, tensile and shear stress/strain curves at small deformations, except for the C_{11}^k which were extracted from the data in Fig. 4. $C_{\alpha\alpha}^k$ with $\alpha \in (1:3)$ are averaged using tensile and compressive tests in α direction, $C_{\alpha\beta}^k$ with α and $\beta \in (1:3)$ from tensile and compressive tests in α and β directions.

Table 3: Elastic constants (in GPa) of the kinked/buckled pyC models and graphite.

Model	C_{11}^k	C_{22}^k	C_{33}^k	C_{44}^k	C_{55}^k	C_{66}^k	C_{12}^k	C_{13}^k	C_{23}^k
Graphite (ZZ)	64	859	32	0.4	0.5	345	38	28	11
RL	77	550	23	7.8	9.7	175	34	28	25
ReL	123	456	21	10.5	14.4	141	63	32	30
ReL$_{1300}$	90	506	26	11.5	16.3	157	68	43	34
ReL$_{1500}$	73	584	26	8.6	12.0	173	66	36	29
ReL$_{1700}$	63	556	24	7.0	8.0	190	57	32	29

The final sets of constants are given in table 3. Aside from the already discussed C_{11}^k, the most affected elastic constants are C_{12}^k and C_{66}^k which show significantly reduced values with respect to C_{12} and C_{66} (see table 2), apart from graphite's C_{66}^k which remains close to C_{66}. Conversely, graphite's C_{13}^k (28 GPa) and C_{23}^k (11 GPa) are significantly larger than C_{13} (4 GPa) while $C_{13}^k \sim C_{13}$ and C_{23}^k a few GPa lower for the pyC models. Similarly, C_{44}^k and C_{55}^k are close to C_{44} for all the models with C_{44}^k slightly lower than C_{55}^k, C_{22}^k are close to C_{11} and C_{33}^k lower than C_{33} by a few GPa.

Delafargue and Ulm (DU) have proposed explicit analytical approximations of the indentation moduli of transverse isotropic or orthotropic materi-

als for conical indenters [43]. For the orthotropic symmetry considered here, the indentation modulus along direction 1, M_1, is given by

$$M_1 = \sqrt{M_{12}M_{13}} \tag{6}$$

where M_{12} and M_{13} read

$$M_{12} = 2\sqrt{\frac{\overline{C_{12}}^2 - C_{12}^2}{C_{22}}\left(\frac{1}{C_{66}} + \frac{2}{\overline{C_{12}} + C_{12}}\right)^{-1}}, \tag{7}$$

$$M_{13} = 2\sqrt{\frac{\overline{C_{13}}^2 - C_{13}^2}{C_{33}}\left(\frac{1}{C_{44}} + \frac{2}{\overline{C_{13}} + C_{13}}\right)^{-1}} \tag{8}$$

and $\overline{C_{\alpha\beta}} = \sqrt{C_{\alpha\alpha}C_{\beta\beta}} > C_{\alpha\beta}$.

Indentation moduli M_1^k obtained with the DU equations using the elastic tensors of the kinked models are shown in Fig. 9. As can be seen, M_1^{DU} values are very close to the corresponding C_{11}^k values, showing the same decrease with increasing heat treatment temperature for the ReL pyC. The slightly lower values, by 14 GPa on average, for M_1^{DU} with respect to C_{11}^k indicates some coupling with other, more compliant, elastic constants during indentation.

Finally, the indentation moduli M_1^{FE} obtained from FEM simulations using the elastic tensors of the kinked models are shown in Fig. 9. The computed indentation curves for the various ReL pyC models are compared to their experimental counterparts in the supporting information (Fig. S4). Aside from graphite, showing a slightly larger value (by 6 GPa), calculated M_1^{FE} values are almost identical (within two GPa difference) to those obtained with the DU method (M_1^{DU}), thus validating the DU approximations for the considered material.

5. Conclusion

We have proposed a detailed investigation of the behavior of high texture pyrocarbons under in-plane compressive load. Nanoindentation experiments performed on a series of materials with L_a in the 2-10 nm range have shown that both indentation modulus and hardness significantly decrease with increasing L_a (or heat treatment temperature). This result was supported and rationalized using a combination of molecular dynamics simulations, based on accurate atomistic models of several of the investigated materials as well as graphite, and finite element modelling of the indentation process. These simulations have permitted to identify the importance of out-of-plane deformations and load transfer during longitudinal compression and complete our common understanding of the indentation process. Especially, MD simulations have shown that the materials undergo a transition from pure in-plane loading at low strains to a much softer response due to the out-of-plane deformation initiated at a critical strain level. These out-of-plane deformations show a transition in nature from kinks in low L_a highly disordered pyCs, to ripplocations in large L_a, highly ordered, carbons. The kinking/buckling transition critical strain was also shown to decrease with increasing order. The evolution of interplanar distance with increasing strain shows that mechanical load is almost entirely transferred to out-of-plane compression in most ordered systems.

It is important here to recall that the kinks observed in this work for the most disordered pyC models are very different from the well-known kink boundaries in graphite [44, 45]. As shown by Freiberg et al. [18], when graphite is compressed in plane, the linear elastic compression regime is fol-

lowed by the reversible nucleation of ripplocations, and then, at much larger strains, by the irreversible conversion of ripplocations into kink boundaries. In this work we have shown that ripplocations nucleation is mostly suppressed in low L_a pyCs, ensuring an extended range of the linear elastic behavior. Instead, in such materials, misoriented domains (i.e. kinks), already existing at rest on the side of extended interlayer cross-links, still allow for elastic softening by reversibly increasing their misorientation angles, yet at larger strains.

Finite elements modeling indicates that critical strain is exceeded in a large volume of the material under the indenter tip, compared to the tip size, proving that most of the mechanical response to indentation is due to material that has undergone the kinking/buckling transition. Applying the FEM using the elastic constants of the kinked/buckled models allows to qualitatively reproduce the evolution of indentation modulus with increasing order. Quantitatively, the obtained moduli remain about 2-3 times larger than experimental ones. Further work is required to reduce the quantitative gap between experiments and simulations; yet, a plausible source of error for the models is their limited size (6 nm) which can probably not fully account for the effect of the kinking/buckling transition on the elastic behavior. Finally, the indentation moduli predicted using FEM were compared to those predicted using the analytical model of Delafargue and Ulm [43]. An almost perfect agreement was obtained, validating this approach, even in the case of such anisotropic materials.

31

CRediT authorship contribution statement

Jean-Marc Leyssale: Conceptualization, Methodology, Formal analysis, Molecular Dynamics Software and Investigation, Data curation, Writing - original draft.

Guillaume Couégnat: Methodology, Formal analysis, Finite element and analytical indentation modelling Investigation, Writing - original draft.

Stéphane Jouannigot: Experimental Investigation, Writing - review & editing.

Gérard Vignoles: Conceptualization, Methodology, Formal analysis, Writing - review & editing, Project management & coordination.

Declaration of competing interest

The authors declare that they have no known competing financial interests or personal relationships that could have appeared to influence the work reported in this paper.

[1] Marx DT, Riester L. Mechanical properties of carbon—carbon composite components determined using nanoindentation. Carbon. 1999;37(11):1679–1684.

[2] Hofmann G, Wiedenmeier M, Freund M, Beavan A, Hay J, Pharr GM. An investigation of the relationship between position within coater and pyrolytic carbon characteristics using nanoindentation. Carbon. 2000;38(5):645–653.

[3] Diss P, Lamon J, Carpentier L, Loubet JL, Kapsa P. Sharp indentation behavior of carbon/carbon composites and varieties of carbon. Carbon. 2002;40(14):2567–2579.

[4] Barsoum MW, Murugaiah A, Kalidindi SR, Zhen T, Gogotsi Y. Kink bands, nonlinear elasticity and nanoindentations in graphite. Carbon. 2004;42(8):1435–1445.

[5] López-Honorato E, Meadows PJ, Xiao P, Marsh G, Abram TJ. Structure and mechanical properties of pyrolytic carbon produced by fluidized bed chemical vapor deposition. Nucl Eng Design. 2008;238(11):3121–3128.

[6] Guellali M, Oberacker R, Hoffmann MJ. Influence of heat treatment on microstructure and properties of highly textured pyrocarbons deposited during CVD at about 1100°C and above 2000°C. Compos Sci Technol. 2008;68(5):1122–1130.

[7] Ozcan S, Tezcan J, Filip P. Microstructure and elastic properties of individual components of C/C composites. Carbon. 2009;47(15):3403–3414.

[8] Gross TS, Timoshchuk N, Tsukrov II, Piat R, Reznik B. On the ability of nanoindentation to measure anisotropic elastic constants of pyrolytic carbon. Z Angew Math Mech. 2013;93(5):301–312.

[9] Zhang H, López-Honorato E, Xiao P. Fluidized bed chemical vapor deposition of pyrolytic carbon-III. Relationship between microstructure and mechanical properties. Carbon. 2015;91:346–357.

[10] Csanádi T, Németh D, Zhang C, Dusza J. Nanoindentation derived elastic constants of carbon fibres and their nanostructural based predictions. Carbon. 2017;119:314–325.

[11] Stein IY, Constable AJ, Morales-Medina N, Sackier CV, Devoe ME, Vincent HM, et al. Structure-mechanical property relations of non-graphitizing pyrolytic carbon synthesized at low temperatures. Carbon. 2017;117:411–420.

[12] Duan S, Liu F, Pettersson T, Creighton C, Asp LE. Determination of transverse and shear moduli of single carbon fibres. Carbon. 2020;158:772–782.

[13] Guruprasad TS, Keryvin V, Charleux L, Guin JP, Arnould O. On the determination of the elastic constants of carbon fibres by nanoindentation tests. Carbon. 2021;173:572–586.

[14] Lamuta C. Elastic constants determination of anisotropic materials by depth-sensing indentation. SN Appl Sci. 2019;1:1263.

[15] Loidl D, Paris O, Burghammer M, Riekel C, Peterlik H. Direct Observation of Nanocrystallite Buckling in Carbon Fibers under Bending Load. Phys Rev Lett. 2005;95:225501.

[16] Gruber J, Lang AC, Griggs J, Taheri ML, Tucker GJ, Barsoum M. Evidence for Bulk Ripplocations in Layered Solids. Sci Rep. 2016;6:33451.

[17] Barsoum MW, Tucker GJ. Deformation of layered solids: Ripplocations not basal dislocations. Scr Mater. 2017;139:166–172.

[18] Freiberg D, Barsoum MW, Tucker GJ. Nucleation of ripplocations through atomistic modeling of surface nanoindentation in graphite. Phys Rev Mater. 2018;2:053602.

[19] Barsoum MW, Zhao X, Shanazarov S, Romanchuk A, Koumlis S, Pagano SJ, et al. Ripplocations: A universal deformation mechanism in layered solids. Phys Rev Mater. 2019;3:013602.

[20] Chen MW, Wu B, Zhou LC, Zhu YB, Wu HA. Micromechanical properties of pyrolytic carbon with interlayer crosslink. Carbon. 2020;159:549–560.

[21] Lafourcade P, Denoual C, Maillet JB. Irreversible Deformation Mechanisms for 1,3,5-Triamino-2,4,6-Trinitrobenzene Single Crystal through Molecular Dynamics Simulations. J Phys Chem C. 2018;122:14954–14964.

[22] Weisbecker P, Leyssale JM, Fischer HE, Honkimäki V, Lalanne M, Vignoles GL. Microstructure of pyrocarbons from pair distribution function analysis using neutron diffraction. Carbon. 2012;50(4):1563–1573.

[23] Farbos B, Weisbecker P, Fischer HE, Da Costa JP, Lalanne M, Chollon G, et al. Nanoscale structure and texture of highly anisotropic pyrocarbons revisited with transmission electron microscopy, image processing, neutron diffraction and atomistic modelling. Carbon. 2014;80:472–489.

[24] Farbos B, Da Costa JP, Vignoles GL, Leyssale JM. Nanoscale elasticity of highly anisotropic pyrocarbons. Carbon. 2015;94:285–294.

[25] Leyssale JM, Da Costa JP, Germain C, Weisbecker P, Vignoles GL. An Image Guided Atomistic Reconstruction of pyrolytic carbons. Appl Phys Lett. 2009;95(23):231912.

[26] Leyssale JM, Da Costa JP, Germain C, Weisbecker P, Vignoles GL. Structural features of pyrocarbon atomistic models constructed from transmission electron microscopy images. Carbon. 2012;50:4388–4400.

[27] Sneddon IN. Boussinesq's problem for a rigid cone. Proc Cambridge Philos Soc. 1948;44(4):492.

[28] Gamboa A, Vignoles GL, Leyssale JM. On the prediction of graphene's elastic properties with reactive empirical bond order potentials. Carbon. 2015;89:176–87.

[29] Farbos B, Freeman H, Hardcastle T, Da Costa JP, Brydson R, Scott AJ, et al. A time-dependent atomistic reconstruction of severe irradiation damage and associated property changes in nuclear graphite. Carbon. 2017;120:111–120.

[30] Brenner DW, Shenderova OA, Harrison JA, Stuart SJ, Ni B, Sinnott SB. A second-generation reactive empirical bond order (REBO) potential energy expression for hydrocarbons. J Phys: Condens Matt. 2002;14(4):783–802.

[31] Stuart SJ, Tutein AB, Harrison JA. A reactive potential for hydrocarbons with intermolecular interactions. J Chem Phys. 2000;112(14):6472–6486.

[32] Allen MP, Tildesley DJ. Computer Simulation of Liquids. Oxford University Press; 1987.

[33] Andersen HC. Molecular dynamics simulations at constant pressure and/or temperature. J Chem Phys. 1980;72:2384.

[34] Berendsen HJC, Postma JPM, van Gunsteren WF, DiNola A, Haak JR. Molecular Dynamics with Coupling to an External Bath. J Chem Phys. 1984;81:3684–3690.

[35] Lees AW, Edwards SF. The computer study of transport processes under extreme conditions. J Phys C. 1972;5:1921–9.

[36] Bolshakov A, Pharr GM. Inaccuracies in Sneddon's Solution for Elastic Indentation by a Rigid Cone and their Implications for Nanoindentation Data Analysis. MRS Proceedings. 1996 Jan;436. Publisher: Cambridge University Press (CUP).

[37] Lafourcade P, Denoual C, Maillet JB. Elastic instability in graphite single crystal under dynamic triaxial compression: Effect of strain-rate on the resulting microstructure. J Appl Phys. 2020;128(4):045101.

[38] Tanguy A, Wittmer JP, Leonforte F, Barrat JL. Continuum limit of amorphous elastic bodies: A finite-size study of low-frequency harmonic vibrations. Phys Rev B. 2002;66:174205.

[39] Rodney D, Tanguy A, Vandembroucq D. Modeling the mechanics of amorphous solids at different length scale and time scale. Model Sim Mater Sci Eng. 2011;19(8):083001.

[40] Obliger A, Valdenaire PL, Capit N, Ulm FJ, Pellenq RJM, Leyssale JM. Poroelasticity of Methane-Loaded Mature and Immature Kerogen from Molecular Simulations. Langmuir. 2018;34(45):13766–13780.

[41] Debyer, freely available diffraction software;. https://github.com/wojdyr/debyer.

[42] Sears VF. Neutron scattering lengths and cross sections. Neutron News. 1992;3(3):26–37.

[43] Delafargue A, Ulm FJ. Explicit approximations of the indentation modulus of elastically orthotropic solids for conical indenters. Int J Sol Struct. 2004;41(26):7351–7360.

[44] März B, Jolley K, Smith R, Wu H. Near-surface structure and residual stress in as-machined synthetic graphite. Materials & Design. 2018;159:103–116.

[45] Alaferdov AV, Savu R, Canesqui MA, Kopelevich YV, da Silva RR, Rozhkova NN, et al. Ripplocation in graphite nanoplatelets during sonication assisted liquid phase exfoliation. Carbon. 2018;129:826–829.